# Inertial Algorithm with Dry Fraction and Convolutional Sparse Coding for 3D Localization with Light Field Microscopy

**Xiaofan Wang[1,2], Zhiyuan Deng[1,2], Changle Wang[1,2], Jinjia Wang[1,2*]**

[1]School of Information Science and Engineering, Yanshan University, China
[2]State Key Laboratory of Integrated Services Networks(Xidian University), Xidian University, China
xy98067376@163.com, 202221040059@stumail.ysu.edu.cn, yswangchangle@163.com, wjj@ysu.edu.cn

## Abstract

Light field microscopy is a high-speed 3D imaging technique that records the light field from multiple angles by the microlens array(MLA), thus allowing us to obtain information about the light source from a single image only. For the fundamental problem of neuron localization, we improve the method of combining depth-dependent dictionary with sparse coding in this paper. In order to obtain higher localization accuracy and good noise immunity, we propose an inertial proximal gradient acceleration algorithm with dry friction, Fast-IPGDF. By preventing falling into a local minimum, our algorithm achieves better convergence and converges quite fast, which improves the speed and accuracy of obtaining the localization of the light source based on the matching depth of epipolar plane images (EPI). We demonstrate the effectiveness of the algorithm for localizing non-scattered fluorescent beads in both noisy and non-noisy environments. The experimental results show that our method can achieve simultaneous localization of multiple point sources and effective localization in noisy environments. Compared to existing studies, our method shows significant improvements in both localization accuracy and speed.

## Introduction

In modern neuroscience, it is fascinating for neuroscientists to understand how the neural networks in the brain process information(Brady et al. 2021). They achieve this by observing and analyzing the activity of neurons in the human brain. Neuronal localization is fundamental to studying information about neuronal activity. With the help of advanced fluorescence metrics, optical microscopy imaging techniques are widely utilized for recording neuronal activity. Despite the advantages of high spatial resolution and potential scalability, large-scale imaging using optical microscopy is quite time-consuming (Weisenburger and Vaziri 2018; Schultz et al. 2016; Aimon et al. 2019).

Light field microscopy (LFM) is considered a highly effective, scan-free imaging technique for observing the location and morphology of large numbers of neurons. It enables real-time observation of the communication dynamics of 3D neuronal networks in the brain (Cong et al. 2017; Song et al. 2022). It drastically reduces the time required for 3D reconstruction compared to conventional scanning imaging techniques and optimized solutions like multiplanar and confocal microscopy (Bai et al. 2022; Song et al. 2020; Pégard et al. 2016; Lu et al. 2023). Ideally, the LFM 3D acquisition rate is limited only by the camera frame rate (Wang et al. 2022).

Broxton et al. (2013) proposed the Richardson-Lucy (R-L) 3D deconvolution algorithm for volume reconstruction, taking into account wave optics theories. This makes the general digital refocusing and 3D deconvolution method (Levoy et al. 2006) applicable in microscopic views. They provided the PSF (point spread function) based on fluctuating optics theory to accurately simulate light field microscopy. However, iterative R-L deconvolution methods suffer from high computational complexity and may also produce reconstruction artifacts (Daube-Witherspoon and Muehllehner 1986; Nöbauer et al. 2017; Lu et al. 2019; Song et al. 2022).

Some approaches employing deep neural networks such as VCD-Net (Wang et al. 2021), LFM-Net (Vizcaíno et al. 2021), learn the model from the training data. These approaches employ both real data and synthetic LFM images to guide the network optimization for better performance (Kai 2019; Li et al. 2019; Wagner et al. 2021; Verinaz-Jadan et al. 2021). However, a purely data-driven approach also has the disadvantage of lacking interpretability and involving too many trainable parameters, which can lead to overfitting and reduced robustness and generalization (Monga, Li, and Eldar 2021). On the other hand, certain strategies for artifact removal (Stefanoiu et al. 2019; Verinaz-Jadan et al. 2020) and optimization algorithms aimed at enhancing spatial resolution and signal-to-noise ratio (Yoon et al. 2020; Nöbauer et al. 2017) attempt to address the limitations of model-based algorithms. Song et al. (2021) proposed a convolutional sparse coding (CSC) LFM model based on the compressive LFM (Pégard et al. 2016). It exploits the feature that EPI (epi-polar plane image) dynamically represents the depth (Liu et al. 2015; Waller, Situ, and Fleischer 2012; Levoy, Zhang, and McDowall 2009) and matches the 3D locations of the target neurons with the sparse codes to generate a synthetic dictionary. It then utilizes translation invariance in phase space for convolutional sparse coding.

Although current CSC models and algorithmic unfolding

*Corresponding author,wjj@ysu.edu.cn (Jinjia Wang)

network can achieve 3D localization of point sources, the accuracy of localization decreases as the depth increases. In microscopic images that closely resemble the real image, it becomes more challenging to distinguish between various sources. We believe that there is a relationship between the alternating direction method of multipliers algorithm (ADMM) used to solve convolutional sparse coding and the tendency of convergence results to fall into local minima (Papyan, Sulam, and Elad 2017; Adly and Attouch 2022; Attouch et al. 2022; Li et al. 2023; Boyd et al. 2011; Zheng et al. 2023). In this paper, our proposed Fast-IPGDF prevents convergence from falling into local minima, balances the algorithm's convergence with its speed, and effectively improves depth matching accuracy. Compared to previous studies, our method not only greatly improves localization accuracy, but also performs well in scenes with noise, and the localization time is further improved.

## 3D Localization

### Epi-polar Plane Image

We followed the modification of the optical instrument in literature (Levoy et al. 2006; Song et al. 2021) to install a custom MLA on the imaging plane of a fluorescence microscope (consisting of a water immersion objective lens and a tube lens). The acquired light field microscope ($25\times, 1.0$ NA) captures the light field information through the camera sensor plane.

The addition of MLA alters the original light field, and the sensor captures images of the light field after the light passes through a series of microlens. The spatial resolution of the LFM system at this point depends on the number of microlens used, while the angular resolution depends on the number of pixels behind each microlens. Each lens in the microlens array functions as a miniature camera positioned at a different location. Behind each of these miniature cameras, a pixel captures an image of the light source from the corresponding angle. As shown on the left side of Figure 2, the $(i, j)$ and $(k, l)$ coordinates denote the relative position of the pixel behind the microlens and the spatial location where that lens is located, respectively.

When EPI is introduced to process the light field image information at the camera sensor plane, the micro-image at the microlens $(k, l)$ in the entire light field image is first selected, and its image block at the coordinate $(i, j)$ is extracted. After indexing the image blocks at coordinates $(i, j)$ within each microlens in this way, the blocks are rearranged according to the location of the microlens $(\cdot, \cdot, k, l)$. The resulting new image, i.e., the sub-aperture image, corresponds to a change in the viewing angle achieved by altering the image block in the center row (or column). The $j - l$ space EPI is generated by fixing a row of the sub-aperture image and then combining the 2D slices from the center of that row (and also in $i - k$ space). This is shown in Figure 2 (Gortler et al. 1996; Wanner, Fehr, and Jähne 2011).

Figure 3 depicts the depth-dependent and shift-invariant properties of EPI. The mathematical equation explains the linear relationship between the slope of the polar line and depth in EPI. When the depth of the point source is fixed,

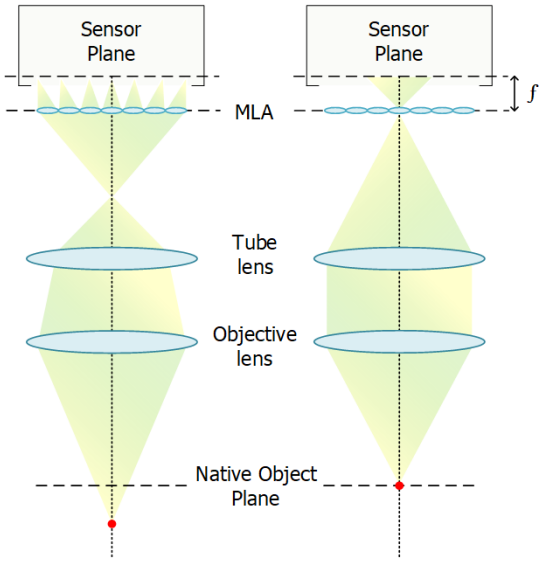


Figure 1: Propagation of the light source (red dot) in the light field at the out-of-focus plane (left) and the in-focus plane (right).

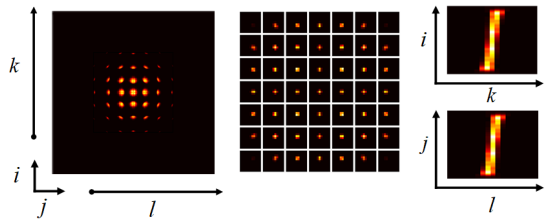


Figure 2: The sensor plane image and EPI.

changing the lateral position of the point source is equivalent to shifting the polar coordinate line along the lateral EPI spatial dimension (Vagharshakyan, Bregovic, and Gotchev 2017).

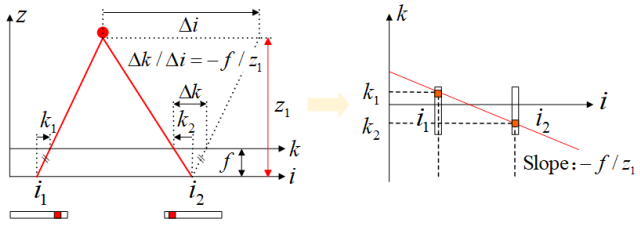


Figure 3: A simplified model of the EPI depth-dependent property.

### Convolutional Sparse Coding Model for EPI-based 3D Localization

The properties of EPI allow us to match the specific depth corresponding to a light field image based on a synthetic dictionary. This is achieved through the variation of the angular view of the light field and the information about the depth

of the incident light. Furthermore, in imammals, the distribution of neurons in their cerebral cortex tends to be consistent and stable. At the same time, the number of neurons per unit volume is sparse, which implies that the EPI is also sparse. These facts enable us to construct a convolutional sparse representation model that captures depth information by observing sparse responses using EPIs. The linear expression for the observed EPI in terms of sparse encoding and depth-dependent dictionary atoms is as follows:

$$Y = \sum_{i=1}^{M} d_i * z_i \tag{1}$$

where $Y \in \mathcal{R}^{\Theta \times N}$ denotes the input EPI, $\Theta$ and N represent angular and spatial dimensions, respectively. $d_i \in \mathcal{R}^{\theta \times n} (\theta \leq \Theta, n \leq N)$ is the $i$-th atom of the EPI dictionary and $z_i \in \mathcal{R}^{\Theta \times N}$ represents sparse code.

The point spread function (PSF) based on wave optics helps to generate a more realistic synthesized light field. On the other hand, the angular detection calibration operation and the MLA center detection operation (Song et al. 2020) result in improved correspondence between the synthesized and detected data. Considering the observed EPIs obtained after these preprocessing operations as input, we propose the convolutional sparse coding problem:

$$\min_{z} \frac{1}{2} \|Y - \sum_{i=1}^{M} d_i * z_i\|_2^2 + \lambda \sum_{i=1}^{M} \|z_i\|_1 \tag{2}$$

We use $l_1$ norm $\|\cdot\|_1$ to regularize the parameters to achieve a sparse solution.

## 3D Location Approach

### Slice-based Convolutional Sparse Coding

Given a signal $\mathbf{y} \in \mathcal{R}^N$, the CSC model represents the signal sparsely through the dictionary as the result of the convolution of convolution kernels $\{\mathbf{d}_i\}_{i=1}^m$ with sparse feature maps $\{\mathbf{Z}_i\}_{i=1}^m \in \mathcal{R}^N$. Due to the shift-invariant property, the internal structure of the signal is not deformed by the need to match the length of the dictionary elements. The convolution process can be equivalently written in the form of matrix multiplication, i.e. $\mathbf{y} = \sum \mathbf{d}_i * \mathbf{Z}_i = \sum \mathbf{D}_i \mathbf{Z}_i$.

Similarly, for a global sparse representation vector $\mathbf{\Gamma} \in \mathcal{R}^{Nm}$ and a local dictionary $\mathbf{D}_L \in \mathcal{R}^{n \times m} (n \ll N)$ consisting of convolution kernels $\mathbf{d}_i$ , we can also equivalently indicate the signal as $\mathbf{X} = \mathbf{D}\mathbf{\Gamma}$, where the global vector $\mathbf{\Gamma}$ consists of the interleaved sparse feature mapping $\{\mathbf{Z}_i\}_{i=1}^m$ and $\mathbf{D}$ is obtained by $N$ shifts of the local dictionary $\mathbf{D}_L$. (Peng 2020) considers that $\mathbf{\Gamma}$ can be viewed as a set of vectors $\alpha_i \in \mathcal{R}^N$ named needles next to each other, indicating that the $m$ convolution operators are aligned with the $i$-th element in $\mathbf{X}$. Define the $i$-th slice $\mathbf{s}_i = \mathbf{D}_L \alpha_i$ of the signal ($\alpha_i$ is assumed to be sparse), then the signal can be represented at this point as:

$$\mathbf{y} = \sum_{i=1}^{N} \mathbf{P}_i^T \mathbf{s}_i = \sum_{i=1}^{N} \mathbf{P}_i^T \mathbf{D}_L \alpha_i \tag{3}$$

where $\mathbf{P}_i^T$ denotes the operation of extracting the $i$-th position of the signal from $\mathbf{Y}$. This approach overcomes the deficiency that the patch-based CSC model tends to ignore the dependencies between individual patches. We can thus obtain the slice-based method formulation of the CSC problem (2) as follows:

$$\min_{\{\alpha_i\}} \underbrace{\frac{1}{2} \|\mathbf{y} - \sum_{i=1}^{N} \mathbf{P}_i^T \mathbf{D}_L \alpha_i\|_2^2}_{} + \lambda \underbrace{\sum_{i=1}^{N} \|\alpha_i\|_1}_{} \tag{4}$$

### IPGDF Algorithm for Slice-based Convolutional Sparse

**IPGDF Algorithm** Consider the structure of $\min_{\mathcal{H}}(f+g)$ in the additive composite case, where $f : \mathcal{H} \to \mathcal{R}$ is a $\mathcal{C}^1$ function with Lipschitz continuous gradient, $\mathcal{H}$ is a real Hilbert space endowed with the associated norm $\|\cdot\|$. $g : \mathcal{H} \to \mathcal{R} \cup \{+\infty\}$ is a convex proper function that is lower semicontinuous.

The forward-backward splitting algorithm was used in (Adly and Attouch 2022) to solve complex function minimization problems, such as the one mentioned above. The inertial dynamics method IPGDF with dry friction is introduced here to improve the convergence of the algorithm. A proof of the convergence of the algorithm is provided in (Adly and Attouch 2022), which relies on the Heavy Ball with Dry Friction Dynamical System associated with the function $f + g$ ($f + g$ is defined as a nonsmooth and nonconvex potential function):

$$\ddot{\mathbf{x}}(t) + \gamma \dot{\mathbf{x}}(t) + \partial \phi(\dot{\mathbf{x}}(t)) + \nabla f(\mathbf{x}(t)) + \partial g(\mathbf{x}(t)) \ni 0 \tag{5}$$

Here: (1) $\gamma \dot{\mathbf{x}}(t)$ represents the viscous damping term, and the viscous damping parameter $\gamma > 0$ ; (2) $\partial \phi(\dot{\mathbf{x}}(t))$ represents the dry friction term, and the friction potential function $\phi = r\|x\|$ satisfies the property (DF)r. Consider a sequence $\mathbf{x}^k$, it satisfies the following proximal-gradient algorithm:

$$\mathbf{x}^{k+1} = \mathbf{x}^k + h \operatorname{prox}_{\frac{h}{1+\gamma h}(\phi + g_k)}(\mathbf{u}^k) \tag{6}$$

where $\mathbf{u}^k = \frac{1}{h(1+\gamma h)}(\mathbf{x}^k - \mathbf{x}^{k-1}) - \frac{h}{1+\gamma h} \nabla f(\mathbf{x}^k)$. The initialized $\mathbf{x}^0, \mathbf{x}^1 \in \mathcal{R}^N$ and the auxiliary function is convex and defined as $g_k(x) := \frac{1}{h} g(\mathbf{x}^k + hx)$. The friction potential function $\phi$ is supposed to be a convex function satisfying (DF) with $B(0, r) \subset \partial \phi(0)$, and $\phi$ is continuous.

*Theorem 1 (Convergence of IPGDF-composite)* Let $f$ and $g$ satisfy the above conditions, and $\inf_{\mathcal{H}}(f+g) > -\infty$. Suppose that the parameters $h > 0, \gamma > 0$ in the algorithm in equation (6) satisfy $h \leq \frac{2\gamma}{L}$. Then for any sequence $(\mathbf{x}^k)$ generated by the algorithm (IPGDF-composite) :

- $\sum_k \left\|\mathbf{x}^{k+1} - \mathbf{x}^k\right\| < +\infty$, $\lim_k \mathbf{x}^k := \mathbf{x}^*$ exists for the strong topology of $\mathcal{H}$;
- The vector $\mathbf{x}^*$ satisfies $0 \in \partial \phi(0) + \nabla f(\mathbf{x}^*) + \partial g(\mathbf{x}^*)$;
- Suppose $\mathcal{H}$ is a finite-dimensional space and $-(\nabla f(\mathbf{x}^*) + \partial g(\mathbf{x}^*)) \in \operatorname{int}(\partial \phi(0))$, then the sequence $(\mathbf{x}^k)$ converges finitely.

**Application to CSC Model** We redefine $f$ and $g$ to incorporate the objective function (4) within the framework of the composite function. As a result, we obtain:

$$f(\alpha_i) = \frac{1}{2}\|\mathbf{y} - \sum_{i=1}^{N} \mathbf{P}_i^T \mathbf{D}_L \alpha_i\|_2^2 \tag{7}$$

$$g(\alpha_i) = \lambda \sum_{i=1}^{N} \|\alpha_i\|_1 \tag{8}$$

Equation (6) shows how to iteratively generate the sequence $\{\alpha_i\}^{k+1}$. And then we can compute the gradient of $f$ as follows:

$$\nabla \alpha_b f\left(\{\alpha_i^k\}\right) = \mathbf{D}_L^T \mathbf{P}_b \left(\mathbf{y} - \sum_{i=1}^{N} \mathbf{P}_i^T \mathbf{D}_L \alpha_i^k\right) \tag{9}$$

Since the $l_1$ regularization is used as the constraint function $g = \|\cdot\|_1$ on $\alpha_i$ in this paper, we define $\phi(x) = r\|x\|_1$ in the framework of the application of the algorithm (IPGDF-composite). The calculation of the proximal mapping, $\text{prox}_{\frac{h}{1+\gamma h}(\phi+g_k)}$ , is transformed into the calculation of $\text{prox}_{r\|x\|_1 + \left\|\frac{1}{h}x^k + x\right\|_1}$.

Simplifying the computation of this proximal mapping, which consists of two separable functions, leads to a one-dimensional calculation. Setting $\lambda = \frac{h}{1+\gamma h}$ = 1, for each $a = \frac{1}{h}x^k \in \mathcal{R}$ :

$$T_a(x) = \arg\min_u \quad \frac{1}{2\lambda}|u - x|^2 + r|u| + |u + a| \tag{10}$$

Since $T_a(x) = -T_{-a}(-x)$, we only need to consider the case that $a \geq 0$ , and the following is the unique solution of equation 10 :

(1) $T_a(x) = x - \lambda(1 + r)$, where $x \geq \lambda(1 + r)$;
(2) $T_a(x) = 0$, where $\lambda(1 - r) \leq x \leq \lambda(1 + r)$;
(3) $T_a(x) = x - \lambda(1 - r)$, where $\lambda(1 - r) - a \leq x \leq \lambda(1 - r)$;
(4) $T_a(x) = -a$, where $-a - \lambda(1 + r) \leq x \leq -a + \lambda(1 - r)$;
(5) $T_a(x) = x + \lambda(1 + r)$, where $x \leq -a - \lambda(1 + r)$;

Finally we obtain the expression for the computation of the proximal gradient $\text{prox}_{\lambda(\phi+g_k)}(x)$ :

$$\left(\text{prox}_{\lambda(\phi+g_k)}(x)\right)_i = \begin{cases} T_{a_i}(x_i) & a_i \geq 0 \\ -T_{-a_i}(-x_i) & a_i \leq 0 \end{cases} \tag{11}$$

with $a_i$ the $i$-th component of the vector $a = \frac{1}{h}x^k \in \mathcal{R}^N$.

**Fast-IPGDF** The Nesterov's accelerated Inertial Gradient method reads as follows, which reduces shocks and oscillations:

$$\begin{cases} z^k = x^k + \eta^k(x^k - x^{k-1}) \\ x^{k+1} = z^k - s \bigtriangledown f(z^k) \end{cases} \tag{12}$$

$s$ denotes the acceleration and $\eta^k$ denotes the learning rate with $0 < \eta^k < 1$. Noting that the temporal discretization of HBDF can correspond to the structure of the acceleration formula above, we have some flexibility in choosing the gradient calculation point $z^k$.

Replace $\bigtriangledown f(x^k)$ with $\bigtriangledown f(z^k)$ in equation (6), where $z^k = x^k + \frac{1}{1+\gamma h}(x^k - x^{k-1})$, we can get the accelerated version of IPGDF:

$$\alpha_i^{k+1} = \alpha_i^k + h\,\text{prox}_{\frac{h}{1+\gamma h}(\phi+g_k)}\left(u_i^k\right) \tag{13}$$

We have $u_i^k = \frac{1}{h(1+\gamma h)}(\alpha_i^k - \alpha_i^{k-1}) - \frac{h}{1+\gamma h} \bigtriangledown f(\alpha_i^k + \frac{1}{1+\gamma h}\left(\alpha_i^k - \alpha_i^{k-1}\right))$.

By adapting *Theorem 1*, we derive the following result ( the convergence proof of our algorithm is similar to the one in (Adly and Attouch 2022) ):

*Theorem 2 (Convergence of Fast-IPGDF)* Let $f$ and $g$ satisfy the conditions mentioned, and $\inf_{\mathcal{H}}(f + g) > -\infty$. Suppose that the parameters $h > 0$, $\gamma > 0$ in *Algorithm 1* satisfy $h \leq \frac{2\gamma}{L}$. Then for any sequence $(\mathbf{x}^k)$ generated by the algorithm (Fast-IPGDF) :

- $\sum_k \left\|\mathbf{x}^{k+1} - \mathbf{x}^k\right\| < +\infty$, $\lim_k \mathbf{x}^k := \mathbf{x}^*$ exists for the strong topology of $\mathcal{H}$;
- The vector $\mathbf{x}^*$ satisfies $0 \in \partial\phi(0) + \bigtriangledown f(\mathbf{z}^*) + \partial g(\mathbf{x}^*)$;
- Suppose $\mathcal{H}$ is a finite-dimensional space and $-(\bigtriangledown f(\mathbf{z}^*) + \partial g(\mathbf{x}^*)) \in \text{int}(\partial\phi(0))$, then the sequence $(\mathbf{x}^k)$ converges finitely.

Algorithm 1: Fast-IPGDF for CSC

**Input**: EPI $\mathbf{Y}$, local convolutional dictionary $\mathbf{D}_L$
**Parameter**: $\alpha_i^0 = \alpha_i^1 \in \mathcal{R}^N, \gamma > 0, h < \frac{2\gamma}{L}$
**Output**: Estimated coding $\alpha_i^K$

1: **while** iteration $k$= 0 : $K - 1$ **do**
2: Compute $\bigtriangledown f\left(\alpha_i^k\right)$ using equation (9).
3: Compute $\text{prox}_{\lambda(\phi+g_k)}(\cdot)$ using equation (11).
4: Update the sparse coding $\{\alpha_i\}^{k+1}$ using equation (13).
5: **end while**
6: **return** solution

## Experiments and Analysis

In this section, we evaluate the 3D localization performance of the proposed Fast-IPGDF method. We compare our method with CSC-based methods in (Song et al. 2020, 2021) to observe the localization effectiveness of the proposed method and the comparison method for single or multiple point sources at different depths. We also compare whether the proposed method is able to achieve accurate localization in the presence of noise interference.

All experiments are conducted on a PC using MATLAB R2018, which is configured with Intel (R) Core(TM) I5-8265U CPU @ 1.6GHz and 4G Byte RAM.

### Experimental Setup

After changing the depth at which the sample is located to obtain the original image representing a specific depth from the EPI image with slopes of different slopes, we can bring

the sparse coefficients of the depth at which the sample is located.

In the selection of experimental subjects, we use static suspension ($5.0 \times 10^3 \mu L^{-1}$) of fluorescent beads with a diameter of 10 $\mu m$ as the experimental samples. These fluorescent beads were sparsely distributed in a piece of agarose gel, serving as ground truth. The original light field images are obtained by gradually varying the depth of the beads and subsequently constructing EPIs according to Part 2 to obtain the sparsity coefficients for the corresponding depths.

Figure 4 shows a partial example of the raw light field images of the fluorescent beads captured by the LFM. It can be observed that as the depth changes, the light field image changes and the slope of the slope line in the constructed EPI is proportional to the depth. The blue spheres in the figure represent the simulated fluorescent beads.

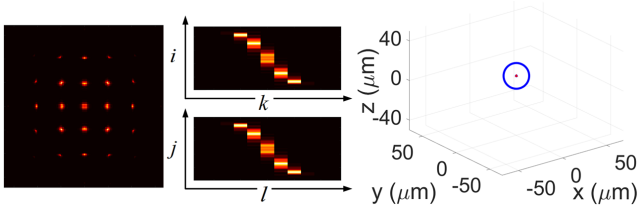


(a) Localization result at +10 $\mu m$ depth

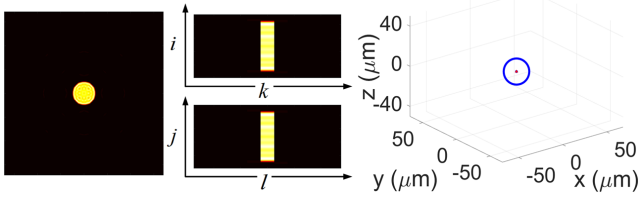


(b) Localization result at 0 $\mu m$ depth

Figure 4: The light field images (left) of the fluorescent beads captured by LFM at depths of +10, 0 $\mu m$ and the corresponding EPIs (middle) and localization results (right), respectively.

## Experimental Results and Analysis

**3D Localization Experiments on Fluorescent Beads** We first test the localization performance of the proposed method using simulated fluorescent beads with a diameter of 10 $\mu m$. Figure 5 shows our localization of fluorescent beads within the depth range of -55 $\sim$ +55 $\mu m$. The blue lines represent the reference positions, while the red circles represent the positions estimated by the algorithms.

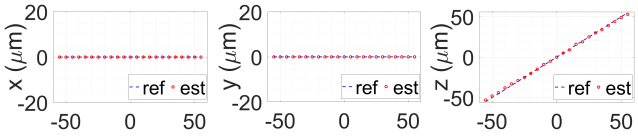


Figure 5: Localization results of Fast-IPGDF in the x, y and z directions within the depth range of -55 $\sim$ +55 $\mu m$.

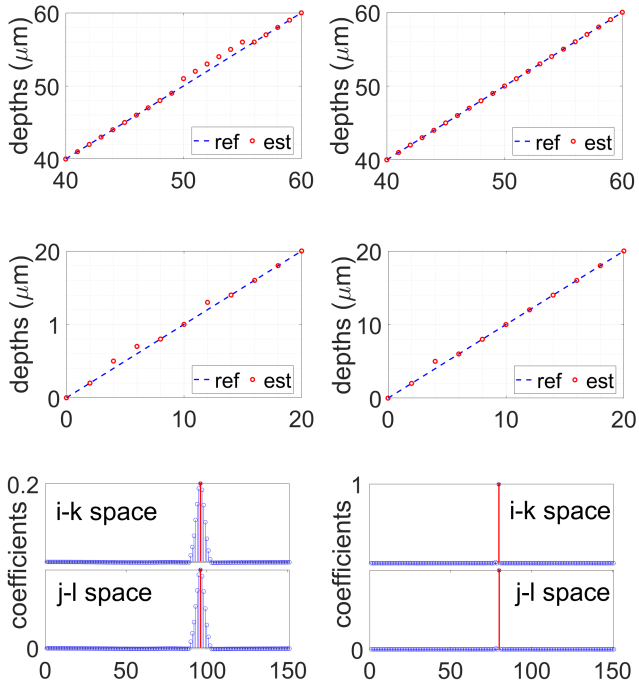


Figure 6: The localization performance of the ADMM-based method (left) and the proposed method (right) in the depth range of 0 $\sim$ +20 $\mu m$ and $+40 \sim$ +60 $\mu m$.

The next issue to be explored is the comparison of the localization performance of the proposed method with the ADMM-based method across different depth ranges. We set the depth ranges to 0 $\sim$ +20 $\mu m$ and $+40 \sim$ +60 $\mu m$ respectively with a simulated fluorescent bead diameter of 10 $\mu m$. As shown in Figure 6, our method is more accurate than the ADMM-based method. This proves that the depth localization effect of our method is more stable at a minimum measurement scale of 1 $\mu m$. It has been proved in (Song et al. 2020, 2021) that the ADMM-based method makes considerable progress in comparison with the CSC method and phase space method, so we only compare with the ADMM-based method for localization accuracy.

| | ADMM-based method | Proposed method |
|---|---|---|
| time cost | 6.489 s | 2.235 s |

Table 1: Average time for processing a single EPI.

Moreover, the proposed method runs about 2.9 times faster compared to the ADMM-based method when processing the same amount of data, which is a considerable improvement when processing large-scale EPI data, further demonstrating the high convergence efficiency of the proposed method.

**Simulate 3D Positioning in Noisy Scenes** The random nature of Poisson noise increases its likelihood to introduce granular interference into the process of reorganizing 4D in-

formation in LFM information. We adjusted the parameters so that the PSNR of the image, after adding the noise, is approximately 24 dB. Ideally, the localization effect of the proposed method and the ADMM-based method is observed within the depth range of -55 $\sim$ +55 $\mu m$.

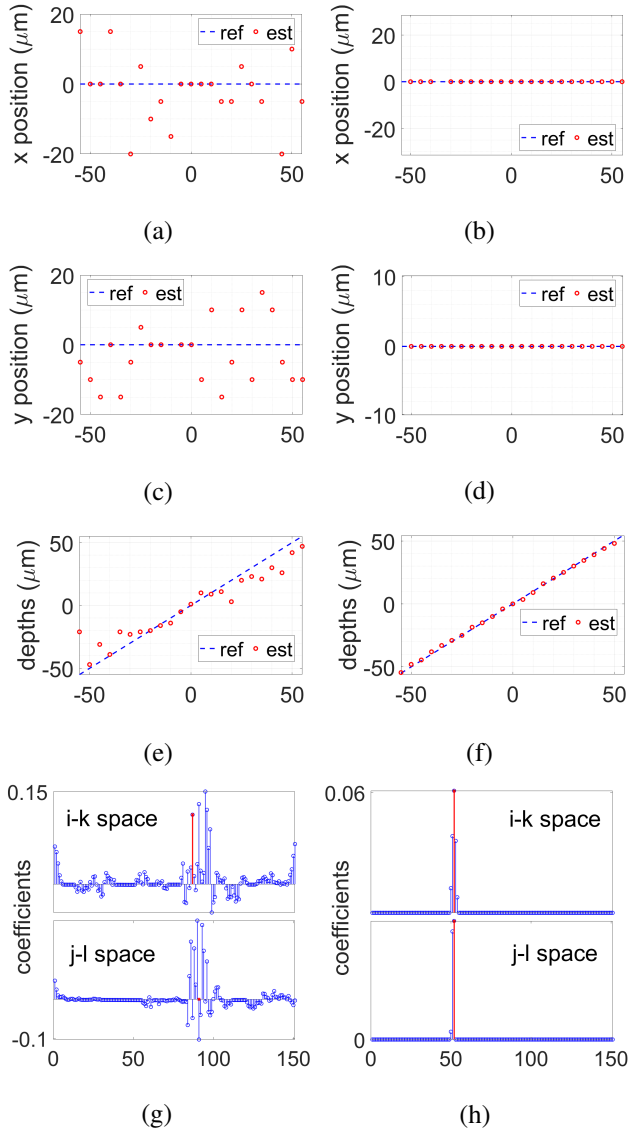


Figure 7: Localization performance of the ADMM-based method (left) and the proposed method (right) in the depth range of -55 $\sim$ +55 $\mu m$ after adding Poisson noise. The localization results for positions $x$, $y$, and $z$ are shown from top to bottom. (g) and (h) show the respective sparse codes found.

The figures (a, c, e, g) in Figure 7 show that the interference of Poisson noise causes the localization curve of the ADMM-based method to fluctuate drastically, resulting in localization failure. This is due to the distortion of the EPI caused by the random noise values of the interfering optical field data during the information rearrangement step in the construction of the EPI. In contrast, the accuracy of the proposed method is slightly degraded, but this effect is relatively minor. Moreover, our method achieves the minimum error in the $x$ and $y$ positions while accurately localizing the depth. This proves that Fast-IPGDF has a fairly good noise immunity. And it is clear that subimages (g) and (h) illustrate that the EPI mapping codes found by Fast-IPGDF are sparser. This shows that Fast-IPGDF exhibits superior convergence performance compared to the ADMM-based method, thereby aiding the localization algorithm in generating highly sparse codes, and so does in Picture 6.

**Multi Light Source Positioning** In order to further demonstrate the depth localization effect of the proposed method, we tested its ability to localize dual light sources. When two light sources at different spatial locations are simultaneously localized, our method is capable of achieving precise localization for both the ideal light source and the simulated 10 $\mu m$ diameter fluorescent beads.

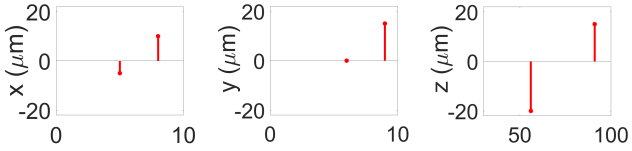


Figure 8: The result of the proposed method for the localization of dual light sources (-10 $\mu m$ and 15 $\mu m$).

**Ablation Experiment** Since the proposed method introduces dry friction, it is necessary to investigate the effect of the parameters in the algorithm on the localization performance of the algorithm. Table 2 gives the RMSEs of the localization results of the proposed method for different values of the dry friction coefficient $r$. The value of $r$ is not chosen to be linearly increasing with the RMSE results, and based on experience we usually choose $r = 0.05$.

| $r$ | 0.01 | 0.03 | 0.05 | 0.07 |
|---|---|---|---|---|
| RMSE ($10^{-6}$) | 2.41 | 2.35 | 2.11 | 2.76 |

Table 2: Effect of different values of the dry friction coefficient $r$.

We also compare the effect of different values of the viscous damping parameter $\gamma$ on the localization results as described in Table 3. During our experiments, we found that an increase of $\gamma$ is accompanied by a demand for the number of iterations, which increases the time taken by the algorithm. Whereas the change of $r$ does not affect the number of iterations.

| $\gamma$ | 10 | 30 | 55 | 65 |
|---|---|---|---|---|
| RMSE ($10^{-6}$) | 2.59 | 2.41 | 3.97 | 5.83 |

Table 3: Effect of different values of the viscous damping parameter $\gamma$.

## Conclusion

In this paper, we propose an improved inertial proximal gradient acceleration algorithm, which makes the proposed method both convergent and efficient via the incorporated dry friction term and the Nesterov acceleration method. The slice-based model speeds up the algorithm iterations and allows us to obtain sparse results much faster. The proposed method achieves excellent results in localization experiments with light field microscopy. Not only does it achieve precise localization at deeper depths, but also shows excellent noise immunity in the presence of noisy situations. Compared with existing methods, our fast localization algorithm demonstrates outstanding noise immunity and depth localization capability.

## Acknowledgments

This work was partly supported by S&T Program of Hebei[grant number 236Z0101G], and the Open Project of State Key Laboratory of Integrated Services Networks (Xidian University)[ grant number ISN24-24]. We thank the referee for their valuable suggestions. We sincerely thank Dr. Pingfan Song for providing valuable coding support and Dr. Bo Xiong for his careful guidance throughout the research process.

## References

Adly, S.; and Attouch, H. 2022. First-order inertial algorithms involving dry friction damping. *Math. Program.*, 193(1): 405–445.

Aimon, S.; Katsuki, T.; Jia, T.; Grosenick, L.; Broxton, M.; Deisseroth, K.; Sejnowski, T. J.; and Greenspan, R. J. 2019. Fast near-whole–brain imaging in adult Drosophila during responses to stimuli and behavior. *PLoS biology*, 17(2): e2006732.

Attouch, H.; Chbani, Z.; Fadili, J.; and Riahi, H. 2022. Fast Convergence of Dynamical ADMM via Time Scaling of Damped Inertial Dynamics. *Journal of Optimization Theory and Applications*, 193.

Bai, L.; Zhang, Z.; Ye, L.; Cong, L.; Zhao, Y.; Zhang, T.; Shi, Z.; and Wang, K. 2022. Volumetric Imaging of Neural Activity by Light Field Microscopy. *Neuroscience Bulletin*, 38(12): 1559–1568.

Boyd, S.; Parikh, N.; Chu, E.; Peleato, B.; and Eckstein, J. 2011. Distributed Optimization and Statistical Learning via the Alternating Direction Method of Multipliers. *Found. Trends Mach. Learn.*, 3(1): 1–122.

Brady, K.; Khorrami, P.; Gjesteby, L.; and Brattain, L. 2021. Instance Segmentation of Neuronal Nuclei Leveraging Domain Adaptation. In *2021 IEEE High Performance Extreme Computing Conference (HPEC)*, 1–5.

Broxton, M.; Grosenick, L.; Yang, S.; Cohen, N.; Andalman, A.; Deisseroth, K.; and Levoy, M. 2013. Wave optics theory and 3-D deconvolution for the light field microscope. *Optics Express*, 21(21): 25418–25439.

Cong, L.; Wang, Z.; Chai, Y.; Hang, W.; Shang, C.; Yang, W.; Bai, L.; Du, J.; Wang, K.; and Wen, Q. 2017. Rapid whole brain imaging of neural activity in freely behaving larval zebrafish (Danio rerio). *Elife*, 6: e28158.

Daube-Witherspoon, M. E.; and Muehllehner, G. 1986. An Iterative Image Space Reconstruction Algorthm Suitable for Volume ECT. *IEEE Transactions on Medical Imaging*, 5(2): 61–66.

Gortler, S. J.; Grzeszczuk, R.; Szeliski, R.; and Cohen, M. F. 1996. The lumigraph. In *Proceedings of the 23rd annual conference on Computer graphics and interactive techniques*, 43–54.

Kai, W. 2019. Deep-learning-enhanced light-field microscopy. *Nature Methods*, 18: 459–460.

Levoy, M.; Ng, R.; Adams, A.; Footer, M.; and Horowitz, M. 2006. Light Field Microscopy. *ACM Trans. Graph.*, 25(3): 924–934.

Levoy, M.; Zhang, Z.; and McDowall, I. 2009. Recording and controlling the 4D light field in a microscope using microlens arrays. *Journal of Microscopy*, 235.

Li, J.; Wei, X.; Li, Q.; Zhang, Y.; Li, Z.; Li, J.; and Wang, J. 2023. Proximal gradient nonconvex optimization algorithm for the slice-based L0-constrained convolutional dictionary learning. *Knowledge-Based Systems*, 260: 110185.

Li, X.; Qiao, H.; Wu, J.; Zhi, L.; Yan, T.; Zhang, R.; Zhang, X.; and Dai, Q. 2019. DeepLFM: Deep Learning-based 3D Reconstruction for Light Field Microscopy. *Biophotonics Congress: Optics in the Life Sciences Congress*.

Liu, H.-Y.; Jonas, E.; Tian, L.; Zhong, J.; Recht, B.; and Waller, L. 2015. 3D imaging in volumetric scattering media using phase-space measurements. *Optics Express*, 23(11): 14461–14471.

Lu, Z.; Liu, Y.; Jin, M.; Luo, X.; Yue, H.; Wang, Z.; Zuo, S.; Zeng, Y.; Fan, J.; Pang, Y.; Wu, J.; Yang, J.; and Dai, Q. 2023. Virtual-scanning light-field microscopy for robust snapshot high-resolution volumetric imaging. *Nature Methods*, 20(5): 735–746.

Lu, Z.; Wu, J.; Qiao, H.; Zhou, Y.; Yan, T.; Zhou, Z.; Zhang, X.; Fan, J.; and Dai, Q. 2019. Phase-space deconvolution for light field microscopy. *Optics Express*, 27(13): 18131–18145.

Monga, V.; Li, Y.; and Eldar, Y. C. 2021. Algorithm unrolling: Interpretable, efficient deep learning for signal and image processing. *IEEE Signal Processing Magazine*, 38(2): 18–44.

Nöbauer, T.; Skocek, O.; Pernia-Andrade, A. J.; Weilguny, L.; Traub, F. M.; Molodtsov, M. I.; and Vaziri, A. 2017. Video rate volumetric Ca2+ imaging across cortex using seeded iterative demixing (SID) microscopy. *Nature Methods*, 14(8): 811–818.

Papyan, V.; Sulam, J.; and Elad, M. 2017. Working Locally Thinking Globally: Theoretical Guarantees for Convolutional Sparse Coding. *IEEE Transactions on Image Processing*, 65(21): 5687–5701.

Pégard, N. C.; Liu, H.-Y.; Antipa, N.; Gerlock, M.; Adesnik, H.; and Waller, L. 2016. Compressive light-field microscopy for 3D neural activity recording. *Optica*, 3(5): 517–524.

Peng, G.-J. 2020. Joint and Direct Optimization for Dictionary Learning in Convolutional Sparse Representation. *IEEE Transactions on Neural Networks and Learning Systems*, 31(2): 559–573.

Schultz, S. R.; Copeland, C. S.; Foust, A. J.; Quicke, P.; and Schuck, R. 2016. Advances in two-photon scanning and scanless microscopy technologies for functional neural circuit imaging. *Proceedings of the IEEE*, 105(1): 139–157.

Song, P.; Jadan, H. V.; Howe, C. L.; Quicke, P.; Foust, A. J.; and Dragotti, P. L. 2020. 3D Localization for Light-Field Microscopy via Convolutional Sparse Coding on Epipolar Images. *IEEE Transactions on Computational Imaging*, 6: 1017–1032.

Song, P.; Jadan, H. V.; Howe, C. L.; Quicke, P.; Foust, A. J.; and Luigi Dragotti, P. 2021. Model-Inspired Deep Learning for Light-Field Microscopy with Application to Neuron Localization. In *IEEE International Conference on Acoustics, Speech and Signal Processing (ICASSP)*, 8087–8091.

Song, P.; Verinaz-Jadan, H.; Howe, C. L.; Foust, A. J.; and Dragotti, P. L. 2022. Light-Field Microscopy for the Optical Imaging of Neuronal Activity: When model-based methods meet data-driven approaches. *IEEE Signal Processing Magazine*, 39(2): 58–72.

Stefanoiu, A.; Page, J.; Symvoulidis, P.; Westmeyer, G. G.; and Lasser, T. 2019. Artifact-free deconvolution in light field microscopy. *Optics Express*, 27(22): 31644–31666.

Vagharshakyan, S.; Bregovic, R.; and Gotchev, A. 2017. Light field reconstruction using shearlet transform. *IEEE transactions on pattern analysis and machine intelligence*, 40(1): 133–147.

Verinaz-Jadan, H.; Song, P.; Howe, C. L.; Foust, A. J.; and Dragotti, P. L. 2020. Volume Reconstruction for Light Field Microscopy. In *IEEE International Conference on Acoustics, Speech and Signal Processing (ICASSP)*, 1459–1463.

Verinaz-Jadan, H.; Song, P.; Howe, C. L.; Quicke, P.; Foust, A. J.; and Dragotti, P. L. 2021. Deep Learning For Light Field Microscopy Using Physics-Based Models. In *IEEE 18th International Symposium on Biomedical Imaging (ISBI)*, 1091–1094.

Vizcaíno, J. P.; Saltarin, F.; Belyaev, Y.; Lyck, R.; Lasser, T.; and Favaro, P. 2021. Learning to Reconstruct Confocal Microscopy Stacks From Single Light Field Images. *IEEE Transactions on Computational Imaging*, 7: 775–788.

Wagner, N.; Beuttenmueller, F.; Norlin, N.; Gierten, J.; Boffi, J. C.; Wittbrodt, J.; Weigert, M.; Hufnagel, L.; Prevedel, R.; and Kreshuk, A. 2021. Deep learning-enhanced light-field imaging with continuous validation. *Nature Methods*, 18(5): 557–563.

Waller, L.; Situ, G.; and Fleischer, J. W. 2012. Phase-space measurement and coherence synthesis of optical beams. *Nature Photonics*, 6(7): 474–479.

Wang, D.; Zhu, Z.; Xu, Z.; and Zhang, D. 2022. Neuroimaging with light field microscopy: a mini review of imaging systems. *The European Physical Journal Special Topics*, 231: 749–761.

Wang, Z.; Zhu, L.; Zhang, H.; Li, G.; Yi, C.; Li, Y.; Yang, Y.; Ding, Y.; Zhen, M.; Gao, S.; et al. 2021. Real-time volumetric reconstruction of biological dynamics with light-field microscopy and deep learning. *Nature methods*, 18(5): 551–556.

Wanner, S.; Fehr, J.; and Jähne, B. 2011. Generating EPI representations of 4D light fields with a single lens focused plenoptic camera. In *Advances in Visual Computing: 7th International Symposium, ISVC 2011, Las Vegas, NV, USA, September 26-28, 2011. Proceedings, Part I 7*, 90–101. Springer.

Weisenburger, S.; and Vaziri, A. 2018. A guide to emerging technologies for large-scale and whole-brain optical imaging of neuronal activity. *Annual Reviews of Neuroscience*, 41: 431–452.

Yoon, Y.-G.; Wang, Z.; Pak, N.; Park, D.; Dai, P.; Kang, J. S.; Suk, H.-J.; Symvoulidis, P.; Guner-Ataman, B.; Wang, K.; and Boyden, E. 2020. Sparse decomposition light-field microscopy for high speed imaging of neuronal activity. *Optica*, 7(10): 1457–1468.

Zheng, Z.; Dai, W.; Xue, D.; Li, C.; Zou, J.; and Xiong, H. 2023. Hybrid ISTA: Unfolding ISTA With Convergence Guarantees Using Free-Form Deep Neural Networks. *IEEE Transactions on Pattern Analysis and Machine Intelligence*, 45(3): 3226–3244.